Non-invasive estimation and control of inlet pressure in an implantable rotary blood pump for heart failure patients

2011 Physiol. Meas. 32 1035

(http://iopscience.iop.org/0967-3334/32/8/004)

Physiol. Meas. **32** (2011) 1035–1060 doi:10.1088/0967-3334/32/8/004

Non-invasive estimation and control of inlet pressure in an implantable rotary blood pump for heart failure patients

A H AlOmari[1,2,3], A V Savkin[1,3], P J Ayre[2], E Lim[4], D G Mason[3,5,6], R F Salamonsen[3,7,8], J F Fraser[3,6,9] and N H Lovell[1,2,3]

[1] Biomedical Systems Laboratory, School of Electrical Engineering and Telecommunications, University of New South Wales, Sydney 2052, Australia
[2] Graduate School of Biomedical Engineering, University of New South Wales, Sydney 2052, Australia
[3] Innovative Cardiovascular Engineering and Technology (ICET) Laboratory, The Prince Charles Hospital, Brisbane, Queensland 4032, Australia
[4] Department of Biomedical Engineering, University of Malaya, Kuala Lumpur 50603, Malaysia
[5] School of Information Technology and Electrical Engineering, University of Queensland, Brisbane, Queensland 4072, Australia
[6] BiVACOR™ Pty Ltd, Brisbane, Queensland 4051, Australia
[7] Department of Intensive Care, Alfred Hospital, Melbourne, Victoria 3800, Australia
[8] Department of Surgery, Monash University, Melbourne, Victoria 3800, Australia
[9] Critical Care Research Group, Intensive Care Unit, The Prince Charles Hospital, and University of Queensland, Brisbane, Queensland 4032, Australia

E-mail: a.savkin@unsw.edu.au and n.lovell@unsw.edu.au

Received 7 December 2010, accepted for publication 12 May 2011
Published 10 June 2011
Online at stacks.iop.org/PM/32/1035

Abstract

We propose a dynamical model for mean inlet pressure estimation in an implantable rotary blood pump during the diastolic period. Non-invasive measurements of pump impeller rotational speed (ω), motor power (P), and pulse width modulation signal acquired from the pump controller were used as inputs to the model. The model was validated over a wide range of speed ramp studies, including (i) healthy (C1), variations in (ii) heart contractility (C2); (iii) afterload (C2, C3, C4), and (iv) preload (C5, C6, C7). Linear regression analysis between estimated and extracted mean inlet pressure obtained from *in vivo* animal data (greyhound dogs, $N = 3$) resulted in a highly significant correlation coefficients ($R^2 = 0.957$, 0.961, 0.958, 0.963, 0.940, 0.946, and 0.959) and mean absolute errors of ($e = 1.604$, 2.688, 3.667, 3.990, 2.791, 3.215, and 3.225 mmHg) during C1, C2, C3, C4, C5, C6, and C7, respectively. The proposed model was also used to design a controller to regulate mean diastolic pump inlet pressure using non-invasively measured ω and P. In the presence of model uncertainty, the controller was able to track and settle to the desired input within a finite number of sampling periods and minimal error (0.92 mmHg). The model developed herein will play a crucial role in

developing a robust control system of the pump that detects and thus avoids undesired pumping states by regulating the inlet pressure within a predefined physiologically realistic limit.

Keywords: implantable rotary blood pump, ventricular assist device, deadbeat controller, inlet pressure estimation, inlet pressure control, pumping states, implantable rotary blood pump control

1. Introduction

Heart failure describes the situation when the cardiac pump function diminishes to such an extent that the heart is unable to deliver adequate oxygenated blood to cope with the body's physiological demands. Whilst medical management of heart failure continues to improve, the optimal treatment for end-stage heart failure remains heart transplantation. However, the deficiency and shortage of donor hearts for transplantation has necessitated the development of a range of mechanical assistance devices for the most critically ill heart failure patients. The implantable rotary blood pumps (IRBPs) have the potential to become a viable long-term treatment option for bridging to heart transplantation or for indefinite support (destination therapy). Small size, minimal blood trauma, and light weight are the most important design aspects which make the second and third generation of IRBPs easily implanted inside the patient's body. This increases the potential for the patients to leave the hospital and resume their normal lives. Rotary blood pumps (RBPs) have been shown to be associated with improved patient health outcomes when compared to the pneumatically driven first generation pulsatile pumps (Slaughter *et al* 2009).

Non-invasive control of IRBPs is one of the most important design goals in providing long-term alternative treatment for congestive heart failure patients. The implantation of additional sensors is not desirable as they result in thrombus formation and require regular calibration due to measurement drifts. This makes the long-term implantation of such left ventricular assist devices (LVADs) problematic. Previously, stable dynamical models to non-invasively estimate the pulsatile flow and differential pressure in an IRBP were proposed and verified using data obtained from pulsatile mock circulatory loop and animal experiments (AlOmari *et al* 2009, Zhang *et al* 2010). The proposed models were successfully used to design a control algorithm for continuous and pulsatile flow (Lim *et al* 2009) using as inputs the non-invasive measurements of pump rotational speed, motor power, and non-invasively estimated flow and differential pressure. The control algorithm was evaluated using a parameter-optimized model of the cardiovascular system-IRBP previously designed and verified in our laboratory (Lim *et al* 2010b). Varying levels of constant and sinusoidal signals together with varying mean, amplitude, and phase shift were applied to the reference pump flow input. Results showed that the pulsatile flow controller was able to track the reference inputs with minimal error in the presence of model uncertainty. Furthermore, the pump flow was shown to settle to the desired reference input within a finite number of sampling periods with minimum steady-state error.

A number of control strategies have been proposed for IRBPs; these can be classified according to the controlled variable. These may include pump differential pressure control (Bullister *et al* 2002, Giridharan and Skliar 2002, Giridharan *et al* 2002); afterload control (Wu *et al* 2003, 2004, 2007); flow control (Lim *et al* 2009, Fu and Xu 2000), and preload control (Choi *et al* 2001). Also control of the pulsatility index of the flow rate

(Vollkron *et al* 2005), motor current signal (Choi *et al* 2001, Endo *et al* 2001), and control of pulsatility gradient (Arndt *et al* 2008, Choi *et al* 2005, Choi *et al* 2007) have been proposed. Most recently, Karantonis *et al* (2010) proposed a control algorithm for a centrifugal IRBP based on a non-invasive indicator of the implant recipient's activity level, with the proposed algorithm being evaluated in a software simulation environment.

In a similar fashion, Choi *et al* (2007) developed a fuzzy logic controller for an axial blood pump based on the blood flow pulsatility which was estimated using a validated pump model. However this used simplified assumptions which included no heart valves, continuous flow throughout the circulatory system, and linear correlation between pump differential pressure, voltage, current, and rotational speed. Waters *et al* (1999) developed a proportional-integral (PI) controller to adjust the motor speed and maintain the system reference differential pressure when changes occurred in the natural heart. Zhou *et al* (1999) used a nonlinear static model of the pump to simulate the hemodynamic responses of the assisted circulatory system as a function of different constant speeds of the pump. They concluded that the model could be used to develop different VAD control algorithms.

Others (Giridharan and Skliar 2006) have used a model-based estimation method to estimate the differential pressure across the pump which was used as an input to a control system of the IRBP. Using a state-space model of the circulatory system together with measurements of pump differential pressure, Wu *et al* (2007) developed their control algorithms to control the aortic pressure. On the other hand, Bullister *et al* (2002) have designed hierarchical control algorithms to control the speed of the pump based on feedback from pressure sensors measuring pump inlet and outlet pressures. Of all these proposed control algorithms, only those based on preload and pulsatility index control have been validated, tested and used in clinical applications (Arndt *et al* 2008). In their study, Arndt *et al* (2008) have proposed a control strategy for IRBPs meeting different user-selectable control objectives using the pulsatility index calculated from pressure difference and the gradient of pulsatility index with respect to pump speed.

Most recently, Saito *et al* (2010) developed a suction release control algorithm for a ventricular assist device by monitoring the inflow cannula pressure using an implantable pressure sensor mounted on the pump. With their control method, the flow assist can be increased more than 15% and suction episodes significantly decreased. Moreover, they claimed that the inflow cannula pressure monitoring was useful not only for the suction detection but also for synchronization with the natural heartbeat.

One limitation of the majority of the previously designed control algorithms was that the estimation of differential pressure and flow were performed using steady-state models without data relating to the transient response of the pump. Furthermore, they required the implantation of additional sensors to provide measurements of parameters used as inputs to their control algorithms.

In heart failure patients with a left ventricle assisted by an IRBP, when the volume in the left ventricle is low, pump inlet pressure will automatically decrease. This may cause suction if the same target speed was maintained. By applying inlet pressure control, target speed will be reduced to allow the inlet pressure to increase and thus avoid suction. In the VentrAssist^{TM} LVAD, during total obstruction of the inlet cannulae, the diastolic inlet pressure may be as low as –160 mmHg, whereas it normally varies between $\pm$10 mmHg during normal pump operation. This is one example that illustrates the benefit of non-invasive estimation and control of inlet pressure during the diastolic period. Also, estimated inlet pressure could be used to provide a definitive input to a controller to prevent highly negative pressure in the left ventricle and thus auto regulates the pump speed to avoid suction. For the first time, in the present study, we used non-invasive measurements of ω, P, together with the pulse width modulation (PWM)

signal as inputs to a novel dynamical autoregressive model with exogenous inputs (ARX) to estimate average inlet pressure during the diastolic period. The resulting model is stable and simple, thus offering a tractable control design solution. The average diastolic inlet pressure estimation model was validated using *in vivo* animal data obtained from acute implantation of a VentrAssist^{TM} LVAD in greyhound dogs under wide ranges of speed ramp studies performed under different operating conditions which includes healthy, variations in heart contractility by administration of a beta blocker (metoprolol), systemic vascular resistance by administration of metaraminol or sodium nitroprusside, and by varying the total blood volume. Also, the model developed herein is used to design a deadbeat controller that non-invasively regulates the diastolic mean inlet pressure of the pump within a predefined physiologically reasonable limit.

2. Materials and methods

2.1. In vivo acute greyhound experiments

The VentrAssist^{TM} (Ventracor Ltd, Sydney, Australia) centrifugal heart pump was acutely implanted in four healthy, anesthetized greyhounds (average weight is 30 kg). In each dog, the inflow pump cannula was inserted into the apex of the left ventricle while the outflow cannula was anastomosed to the ascending aorta. The dogs were instrumented with indwelling catheters (DwellCath, Tuta Labs, Lane Cave, NSW, Australia) to measure the left ventricular (P_{lv}), left atrial (P_{la}), aortic (P_{ao}), pulmonary arterial (P_{pa}), central venous (P_{cv}), pump inlet (P_{in}) and outlet (P_{out}) pressures. Pump (Q_p) and aortic valve (Q_{ao}) flows were measured by ultrasonic flow probes (Transonic Systems Inc., Ithaca, NY, USA). P_{in} was obtained from a point very close to the inlet of the pump, also Q_p and P_{out} were obtained near the outlet of the pump and not at the distal ends of the pump cannulae. Furthermore, the instantaneous values of ω, motor current (I), supply voltage (V), and PWM were continuously monitored from the pump controller and recorded for further analysis. All the aforementioned signals were recorded using a Powerlab data acquisition system (ADInstruments, Castle Hill, NSW, Australia). In all dog experiments, the pump implantation was executed carefully without significant arrhythmias or blood loss.

Intervals of approximately 30 min were allowed to stabilize all hemodynamic parameters. A speed ramp study for 'healthy condition' (C1) was performed. In this study, the pump outflow cannula was first occluded to record the baseline hemodynamic parameters. Then, after releasing the occlusion, the impeller speed was increased from 1250 to 2950 rpm in 100 rpm increments. At the end of the experiment, speed of the pump was turned down to 1600 rpm and blood samples were taken for measurements of the hematocrit (HCT) values and blood gas analysis purposes.

This was followed by the administration of a cardiodepressant; beta-adrenoreceptor blocker drug (metoprolol) through the venous line to mimic acute heart failure conditions and reduces the cardiac contractility. Metoprolol is a beat-adrenergic blocking agent, which reduces or inhibits the stimulant effect of catecholamines on the beta receptors of the heart which leads to the decrease in heart rate, cardiac contractility and cardiac output. Metoprolol was administrated in small sequential aliquots (up to 5 mg) to avoid excessive hemodynamic responses. The beta blocker (metoprolol) was administrated until the total cardiac output fell to approximately 50% of the 'healthy condition', or until the aortic pressure (P_{ao}) dropped below 60 mmHg. Next, a speed ramp test for the 'heart failure: reduced heart contractility-afterload low' (C2) was performed.

After that, an afterload dependence studies were executed by administration of a potent sympathomimetic drug with vasoconstrictive action drug 'metaraminol' (solution containing 10 mg of metaraminol diluted in 20 mL of fluid). This drug increases the afterload by directly acting on the vessels through alpha adrenergic receptors, leading to an increase in the systolic and diastolic blood pressure, thus increasing the afterload as seen by the ventricle. Metaraminol was continuously infused at a fixed rate (from 1.5–3 μg kg^{-1} min^{-1}), depending on the conditions of each animal, to guarantee the consistency of afterload during each speed ramp test. The metaraminol infusion rate was first chosen to increase the P_{ao} by approximately 20 mmHg higher compared with case C2. Once this was reached and after all hemodynamic parameters were reached their steady states, a speed ramp test for the 'heart failure: reduced heart contractility-afterload medium' (C3) was executed. This was also repeated for another level of afterload, with 'heart failure: reduced heart contractility-afterload high' (C4), at mean P_{ao} of 20 mmHg higher compared with case C3. The vasodilator sodium nitroprusside was administrated whenever mean blood pressure was excessively increased.

After stopping of metaraminol infusion, preload dependence tests were carried out. The rate of a cardiotomy suction machine was varied to change the total blood volume. A speed ramp tests with 'heart failure: reduced heart contractility-preload low (C5)', 'heart failure: reduced heart contractility-preload medium (C6)', and 'heart failure: reduced heart contractility-preload high (C7)' were performed. Gelofusine was used as the fluid medium to reduce the rate of blood volume leakage into the interstitial tissue because it has a higher oncotic pressure than plasma. In each volume level, each dog underwent several speed ramp tests in which impeller speed was increased from 1250 to 2950 rpm in a stepwise increment of 100 rpm with each step lasting for 30 s. The sampling rate was set at 4 kHz for data recordings, but, in further analysis, the data were down-sampled to 50 Hz.

2.2. Diastolic period extraction

Inlet pressure signals were processed by an algorithm that detects the onset and the end of the cyclic diastolic periods. We used the method proposed by Zong *et al* (2003) where an algorithm was proposed to detect the beginning of the arterial blood pressure pulses. The performance of the pulse detection algorithm resulted in 99.31% of accuracy when evaluated using the MIT-BIH Polysomnographic Database (Zong *et al* 2003). To summarize, the inlet pressure signal (P_{in}) has to pass three stages: a windowed and weighted slope sum function (*ssf*) to support and enhance the upslope and suppress the remainder of the signal, an edge detector of the rectified and processed *ssf* followed by a threshold and decision rule. P_{in} signal was processed using the *ssf* which included two processes where the filtered signal was differentiated and then summed to enhance the upslope and suppress the remainder of the signal. The *ssf* at time k is defined as follows (Zong *et al* 2003):

$$ssf(k) = \sum_{j=k-\mu}^{k} \Delta y_j, \tag{1}$$

where

$$\Delta y_j = \begin{cases} \Delta P_{\text{in}} & \text{if} \quad \Delta P_{\text{in}} > 0 \\ 0 & \text{if} \quad \Delta P_{\text{in}} \leqslant 0, \end{cases} \tag{2}$$

and μ is the number of samples representing the analyzing window of the first derivative of the inlet pressure signal ΔP_{in} where $\Delta P_{\text{in}} = P_{\text{in}_j} - P_{\text{in}_{j-1}}$. μ was chosen to be 32 samples which is equal to the upslope of P_{in}. After that, the *ssf* was rectified by a suitable threshold value to suppress small amplitudes before an edge detector, and decision rules were applied

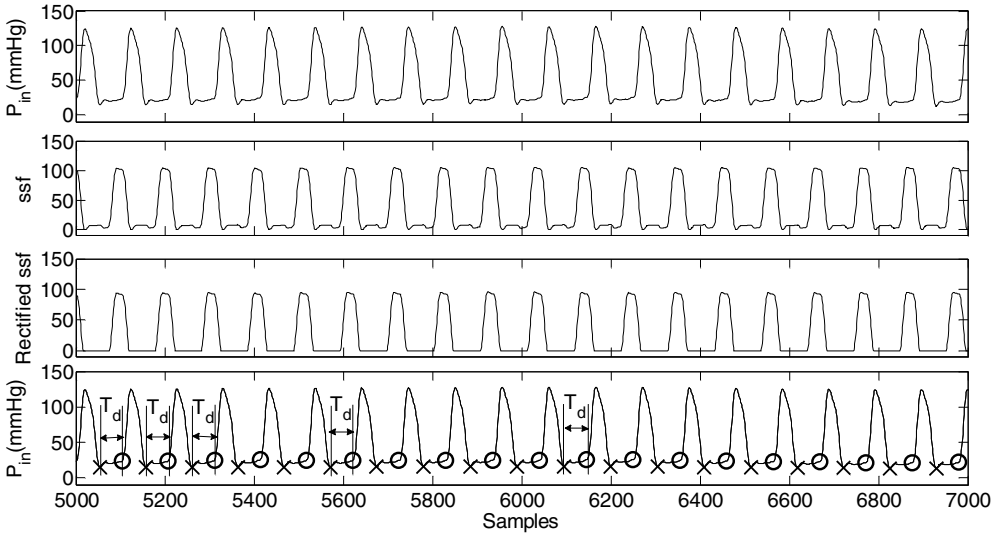

Figure 1. Relationship between the inlet pressure signal (P_{in}) and *ssf* signal together with the extracted diastolic period (T_d) where 'x' and 'o' represent the starting and the end of the diastolic period, respectively.

to extract the diastolic periods of all inlet pressure signals. The relation between P_{in} and the *ssf* signals together with extracted diastolic period (T_d) is shown in figure 1.

2.3. System identification and data analysis

Recorded P_{in}, P, ω, and PWM signals obtained from each animal data were averaged during T_d of the heart. Average values of all signals were stored for further analysis and system identification. Data were divided into two sets: one set was used for system identification, while another set was used to validate the model. The first set of data consisted of one animal experiment corresponding to the healthy, three afterload and preload tests, while the other set contained data from the other three greyhound experiments. In both, identification and validation data sets, the changes in the pump target speed were included in the data so that the transient response of the mean diastolic pump inlet pressure could be identified.

In the system identification process, an off-line least-squares method (Ljung 1999) was used to estimate the parameter coefficients of the mean diastolic inlet pressure estimation model. Values of parameter coefficients were chosen so that the error between the estimated and measured signals was minimized. The output model order (n) together with the model inputs orders (m) was chosen across a range of 1–10. The *delay value* was determined by estimating the impulse response of the system using cross-correlation analysis between the inputs and output signals. The mean absolute error (e) and correlation coefficient (R) between estimated ($\hat{\bar{P}}_{\text{in}}(kh)$) and measured ($\bar{P}_{\text{in}}(kh)$) mean inlet pressures during T_d were used to check the performance and to evaluate the estimation accuracy of the system models. Values of e and R were evaluated as follows:

$$e = \frac{1}{N}\sum_{i=1}^{N}(\bar{P}_{\text{in}}(kh) - \hat{\bar{P}}_{\text{in}}(kh))^2, \tag{3}$$

$$R = \frac{\sum_{i=1}^{N} (\bar{P}_{\text{in}}(kh) - \bar{P}_{\text{in}})(\hat{\bar{P}}_{\text{in}}(kh) - \hat{\bar{P}}_{\text{in}})}{\sqrt{\sum_{i=1}^{N} (\bar{P}_{\text{in}}(kh) - \bar{P}_{\text{in}})^2 \sum_{i=1}^{N} (\hat{\bar{P}}_{\text{in}}(kh) - \hat{\bar{P}}_{\text{in}})^2}}. \tag{4}$$

Here, N is the length of data, $\hat{\bar{P}}_{\text{in}}$ and $\bar{P}_{\text{in}}$ are the mean values of the estimated and measured signals, respectively.

To reduce the contributions of external sources in the identification process of the system, all sets of data were explicitly pre-treated to remove trends and offsets by direct subtraction. All simulations, linear regression analysis, model implementation and algorithms were performed in MATLAB R2007b® (The Mathworks, Inc., Natick, MA, USA). The models were implemented on a PC running Windows XP.

2.4. Dynamical modeling

A steady-state, non-invasive flow (Q_{ss}) estimator was designed in a non-pulsatile mock loop environment for the IRBP. The static equation for Q_{ss} which uses as inputs the input power (P) and pump rotational speed (ω) is based on the work of Malagutti *et al* (2007) and Ayre *et al* (2003) and is of the following form:

$$Q_{ss} = a_0 + a_1 P + a_2 P^2 + a_3 P^3 + b_1 \omega + b_2 \omega^2. \tag{5}$$

Here, P = VI is the product of supply voltage (V) and motor current (I), ω is the impeller rotational speed of the pump, a_0, b_1, and b_2 are constants and power coefficients a_1, a_2, and a_3 were described as having linear function of viscosity levels (Malagutti *et al* 2007). A significant relationship between HCT and the power coefficients was identified. This is because higher values of HCT correspond to more viscous blood, raising the necessary power to run the pump. In contrast, the coefficients of speed and the offset term (a_0) indicated no apparent dependence on HCT (Malagutti *et al* 2007).

Now, we introduce a variable $\bar{f}(kh)$ as follows:

$$\bar{f}(kh) = g(\bar{P}(kh), \bar{\omega}(kh)), \tag{6}$$

where

$$g(\bar{P}(kh),\ \bar{\omega}(kh)) = \sum_{i=0}^{3} a_i \bar{P}^i(kh) + \sum_{j=1}^{2} b_j \bar{\omega}^j(kh). \tag{7}$$

Here, k is the discrete time satisfying $t = kh$ and $h > 0$ is the sampling interval equal to 0.02 s, $\bar{P}(kh) = \bar{V}(kh)\bar{I}(kh)$ is the product of average supply voltage ($V(kh)$) and motor current ($I(kh)$), and $\bar{\omega}(kh)$ is the average pump rotational speed during T_d. In other words, the variable $\bar{f}(kh)$ represents the right-hand side of the static equation (5) but values of $\bar{\omega}(kh)$ and average power ($\bar{P}(kh)$) during extracted T_d were used as inputs.

We introduce a multi-input dynamical ARX model to estimate mean inlet pressure ($\hat{\bar{P}}_{\text{in}}(kh)$) during T_d as follows (AlOmari *et al* 2010):

$$\hat{\bar{P}}_{\text{in}}(kh) + \sum_{i=1}^{n} z_i \hat{\bar{P}}_{\text{in}}([k-i]h) = \sum_{j=1}^{4} \sum_{i=1}^{m_j} x_{ij} u_j([k - d_j - i + 1]h) + e_1(kh), \tag{8}$$

where $\hat{\bar{P}}_{\text{in}}(kh)$ is the output of the system which represents the estimated mean inlet pressure during T_d of the cardiac cycle, n is the model output order, m_j is the model inputs order, d_j is the delay value, i.e. the number of samples that occur before the input affects the output, z_i and x_{ij} are the output and input parameters of the model, respectively, $e_1(kh)$ represents the model error, and $u_j(kh)$ are four exogenous inputs defined as follows:

$$u_1(kh) = \overline{P}(kh), \tag{9}$$

$$u_2(kh) = \sqrt{\overline{\omega}(kh)}, \tag{10}$$

$$u_3(kh) = \overline{f}(kh), \tag{11}$$

$$u_4(kh) = \overline{\mathrm{PWM}}(kh)\overline{f}(kh). \tag{12}$$

Here, $\bar{P}(kh)$ and $\bar{\omega}(kh)$ are the mean motor power and pump rotational speed, respectively, $\bar{f}(kh)$ is the steady-state nonlinear average flow estimator, and $\overline{\mathrm{PWM}}(kh)$ is the mean pulse-width modulation signal during T_d of the heart. We assume that $m_1 = m_2 = \cdots = m_4 = m$. Also, $d_1 = d_2 = \cdots = d_4 = 2$ was determined.

Values of parameter coefficients of the mean inlet pressure estimation model described in (8) were identified using the system identification algorithm described in subsection 2.3. Parameters were chosen so that the error between $\hat{\bar{P}}_{\mathrm{in}}(kh)$ and $\bar{P}_{\mathrm{in}}(kh)$ was minimized. The performance of the model for mean inlet pressure estimation given in equations (8)–(12) was evaluated based on the mean absolute error e, equation (3), and correlation coefficient R, equation (4), for different combinations of model inputs orders and model output order. Also, model orders n, m and delay values were chosen so that e was minimized with maximum R between $\hat{\bar{P}}_{\mathrm{in}}(kh)$ and $\bar{P}_{\mathrm{in}}(kh)$.

2.5. Controller design and implementation

The high variability in the preload and afterload encountered by patients during their daily activities places restrictions on the control design problem for an IRBP as it is required that the controller should react rapidly to these changes in order to avoid undesired pumping states such as suction which may result in ventricular collapse. In order to track the desired reference input signal ($r(kh)$) within minimum possible sampling periods and minimum steady-state error, in this paper, we propose a deadbeat controller (see e.g. Åström and Wittenmark 1997, page 17). The deadbeat control algorithm guarantees that for a noise-free system ($e_1(kh) \equiv 0$), in (8), it follows that $\hat{\bar{P}}_{\mathrm{in}}(kh) = r(kh)$. Deadbeat control is a control strategy in which the system is at rest when the desired reference input is reached (see e.g. Åström and Wittenmark 1997, page 17). For linear systems, the steady-state deadbeat (pole-placement) controller is linear while it should be nonlinear for a nonlinear system.

Now, we derive our actual control input signal, $u(.)$, which represents the mean real control input signal (pulse width modulation signal ($\overline{\mathrm{PWM}}(.)$) during T_d), based on equations (8)–(12) as follows:

$$u(kh) = \frac{1}{x_{14}u_3(kh)} \left[\begin{array}{l} \displaystyle\sum_{i=1}^{n} z_i \hat{\bar{P}}_{\mathrm{in}}([k-i]h) - \sum_{j=1}^{3}\sum_{i=1}^{m} x_{ij}u_j([k-d_j-i+1]h) \\ \qquad \displaystyle - \sum_{q=2}^{3} x_{q4}u_4([k-d_j-q+1]h) + r([k+2]h) \end{array} \right], \tag{13}$$

where z_i, x_{ij} are constant parameters to be identified using the system identification algorithm described in subsection 2.3, u_j are the three exogenous measured inputs defined previously in equations (9)–(11), and $r(kh)$ is the desired reference input. In this study, the nonlinearity of control input (13) is a result of the nonlinear flow estimator $\bar{f}(kh)$ defined in (6) resulting in a nonlinear system represented in equations (8)–(12). For a given operating rotational speed, the cubic polynomial in equation (5) and thus in equations (6) and (7) highlights the nonlinear nature of the relationship between pump power and actual pump flow in the VentrAssist$^{\mathrm{TM}}$ IRBP. Unlike other RBPs, the identified linear relationship between

output flow rate and input electrical power (see e.g. Wakisaka *et al* 1997, and Yoshizawa *et al* 2002) is not applicable to the VentrAssist^{TM} and that the nonlinear flow estimator (equations (5)–(7)) provides a much more accurate interpolation especially at low and high flow rates (Malagutti *et al* 2007, Ayre *et al* 2003).

In the present study, although measured values of pump power and rotational speed were used as inputs to the diastolic mean inlet pressure estimation model (8) and the deadbeat controller algorithm, we also simulate their values to initiate the control algorithm as it uses two-step ahead predictor for values of power and pump speed. Also, the simulation of the instantaneous values of the pump speed and power made it easy to study the dynamics and transient responses of the mean diastolic inlet pressure estimation model during variations in healthy, preload, afterload and contractility of the heart. In order to implement the control algorithm, two new ARX models were developed to simulate values of mean motor power and pump rotational speed. The first one describes the relationship between the mean real control input, i.e. the $\overline{\mathrm{PWM}}(.)$ signal ($u(.)$), the mean steady-state pump flow ($\bar{f}(.)$), mean pump rotational speed ($\bar{\omega}(.)$), mean inlet pressure ($\bar{P}_{\mathrm{in}}(.)$), and average motor power ($\bar{P}(.)$) during the diastolic period (T_d). The resulting system model is used to simulate values of mean pump power ($\hat{\bar{P}}(kh)$) during T_d and is described by the following difference equation:

$$\begin{aligned}\hat{\bar{P}}(kh) = {} & d_1\overline{\mathrm{PWM}}([k-1]h) - d_2\overline{\mathrm{PWM}}([k-2]h) - d_3\bar{\omega}([k-1]h) + d_4\bar{\omega}([k-2]h) \\ & - d_5\bar{f}([k-1]h) + d_6\bar{f}([k-2]h) - d_7\bar{P}_{\mathrm{in}}([k-1]h) + d_8\bar{P}_{\mathrm{in}}([k-2]h) \\ & + d_9\bar{P}([k-1]h) - d_{10}\bar{P}([k-2]h) + d_{11}\bar{P}([k-3]h) + e_2(kh). \end{aligned} \tag{14}$$

Here $d_1 - d_{11}$ are parameter coefficients.

Also, during T_d, a second ARX model which relates the mean control input, i.e. the $\overline{\mathrm{PWM}}(.)$ signal ($u(.)$), the mean steady-state pump flow ($\bar{f}(.)$), mean pump rotational speed ($\bar{\omega}(.)$), mean inlet pressure ($\bar{P}_{\mathrm{in}}(.)$), and mean motor power ($\bar{P}(.)$) was identified and used to simulate values of the mean rotational pump speed. The resulting model used to simulate the mean pump rotational speed ($\hat{\bar{\omega}}(kh)$) is also described by the following difference equation:

$$\begin{aligned}\hat{\bar{\omega}}(kh) = {} & g_1\overline{\mathrm{PWM}}([k-3]h) + g_2\overline{\mathrm{PWM}}([k-4]h) + g_3\bar{P}([k-3]h) - g_4\bar{P}([k-4]h) \\ & + g_5\bar{f}([k-3]h) + g_6\bar{f}([k-4]h) + g_7\bar{P}_{\mathrm{in}}([k-3]h) - g_8\bar{P}_{\mathrm{in}}([k-4]h) \\ & + g_9\bar{\omega}([k-3]h) - g_{10}\bar{\omega}([k-4]h) + e_3(kh), \end{aligned} \tag{15}$$

where g_1–g_{10} are parameter coefficients.

Parameter coefficients, orders, and time delays for the two-step ahead predictors of power (14) and pump speed (15) were derived using the identification procedure described in subsection 2.3. Here, again, experimental data were divided into two sets: one set was used for identification while another set was used to test the predictors. Orders and parameters were chosen so that the mean absolute errors (e), obtained from (3), between the estimated and measured values were minimized. In all simulations, we added uniformly distributed noise to model errors term $e_1(kh)$–$e_3(kh)$ to represent model uncertainty.

In the present study, the deadbeat controller algorithm was implemented to control the mean diastolic inlet pressure. The input to the deadbeat controller is the reference mean diastolic inlet pressure (r), estimated mean diastolic inlet pressure ($\hat{\bar{P}}_{\mathrm{in}}$), predicted mean diastolic pump power ($\hat{\bar{P}}$), and predicted mean diastolic pump rotational speed ($\hat{\bar{\omega}}$) while the output of the controller is the diastolic mean pulse width modulation $\overline{\mathrm{PWM}}$ to the rotary pump, represented as ($u(.)$). The overall structure of the model and controller is illustrated in the block diagram shown in figure 2.

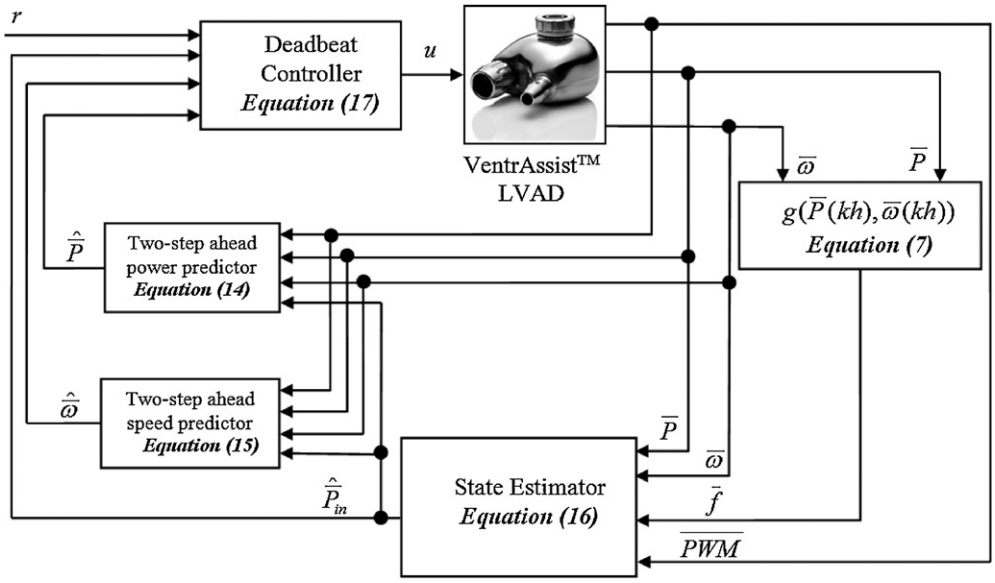

Figure 2. Block diagram of the deadbeat control system developed for non-invasive control of the mean diastolic inlet pressure in a LVAD.

3. Results

The performance of the mean inlet pressure estimation model given in equation (8) was evaluated based on the mean absolute error e, equation (3), and correlation coefficient R, equation (4), for different combinations of model input order m and model output order n. System model orders of $n = 3$, $m = 3$, and $d_1 = d_2 = \cdots = d_4 = 2$ gave the best results, i.e. with the minimal e and highest R values between estimated and measured mean inlet pressure.

The resulting system model is described by the following difference equation:

$$\hat{\hat{P}}_{\text{in}}(kh) = \sum_{j=1}^{4}\sum_{i=1}^{3} x_{ij}u_j([k-d_j-i+1]h) - \sum_{i=1}^{3} z_i \hat{\hat{P}}_{\text{in}}([k-i]h) + e_1(kh). \tag{16}$$

Also, based on (13), the resulting control input signal is as follows:

$$u(kh) = \frac{1}{x_{14}u_3(kh)} \left[\begin{array}{l} \displaystyle\sum_{i=1}^{3} z_i \hat{\hat{P}}_{\text{in}}([k-i]h) - \sum_{j=1}^{3}\sum_{i=1}^{3} x_{ij}u_j([k-2-i+1]h) \\ \qquad \displaystyle - \sum_{q=2}^{3} x_{q4}u_4([k-2-q+1]h) + r([k+2]h) \end{array} \right]. \tag{17}$$

Here, z_1, z_2, z_3 are constants with values of -1.119, 0.580, and -0.447, respectively. Also, x_{11}, x_{12}, x_{13}, x_{14}, x_{21}, x_{22}, x_{23}, x_{24}, x_{31}, x_{32}, x_{33}, and x_{34} are constants with values of -0.92625, -0.51517, 0.10963, -0.00665, 0.46835, 0.36252, 0.53844, -0.01216, 0.46272, -0.20972, -0.47741, and 0.00987, respectively; u_j represents the four exogenous inputs described previously by equations (9)–(12).

The dashed lines in the upper panels of figures 3(A), 4(A) and 5(A) show the estimated and measured mean diastolic P_{in} in the three greyhound experiments during the speed ramp

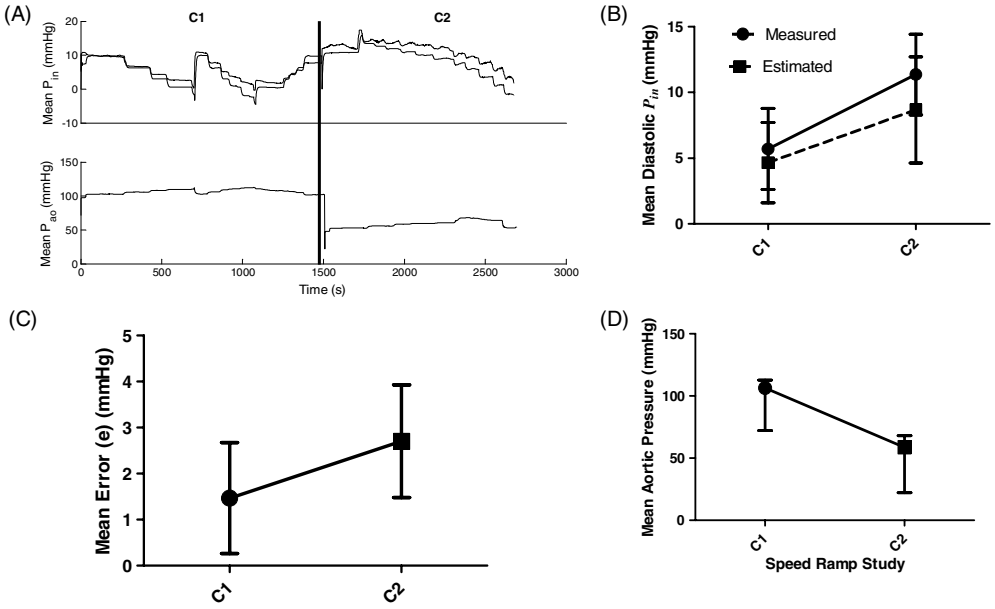

Figure 3. (A) $\hat{\bar{P}}_{\text{in}}(kh)$compared with $\bar{P}_{\text{in}}(kh)$ obtained from the first greyhound experiments during healthy condition (C1) and from after metoprolol was infused (C2) together with (B) comparison between estimated versus measured mean P_{in} obtained during C1 and C2, and (C) comparison between estimation errors obtained during speed ramp tests C1 and C2 in the first greyhound. (D) Mean aortic pressure/afterload variations. In both C1 and C2, target rotational speed was varied from $\omega = 1250$ to 2950 rpm. The solid line shows the measured $\bar{P}_{\text{in}}(kh)$, while the dashed line shows $\hat{\bar{P}}_{\text{in}}(kh)$.

tests C1 and C2. The variations in the mean aortic pressure ($\overline{P_{ao}}$) for each dog during speed ramp tests C1 and C2 are also shown in the lower panels of figures 3(A), 4(A), and 5(A), respectively. The comparison between $\hat{\bar{P}}_{\text{in}}(kh)$ together with $\bar{P}_{\text{in}}(kh)$ obtained from each greyhound experiment during C1 and C2 is also shown in figures 3(B), 4(B), and 5(B). Moreover, the mean absolute error (e) during each speed ramp experiment for each greyhound during C1 and C2 were compared in figures 3(C), 4(C), and 5(C). Note that the model was able to accurately track the changes in $\bar{P}_{\text{in}}(kh)$ with stable transient response when afterload was significantly dropped from after metoprolol infusion (C2) (figures 3(D), 4(D), and 5(D)).

As noticed, the mean diastolic P_{in} estimation model was able to accurately estimate the mean diastolic measured P_{in} with stable transient response during healthy (C1) and from after reduced heart contractility (C2) which caused the aortic pressure to significantly drop together with heart rate. During the metoprolol infusion, P_{ao} was dropped almost below 60 mmHg; this affects the accuracy of the mean diastolic P_{in} estimation model as the mean absolute error (e) between $\hat{\bar{P}}_{\text{in}}(kh)$ and $\bar{P}_{\text{in}}(kh)$ was increased. Tables 1 and 2 summarize the values of mean diastolic estimated and measured P_{in}, mean P_{ao}, e, and correlation coefficient (R^2) obtained from each animal experiment during C1 and C2 speed ramp tests. Linear regression analysis between $\hat{\bar{P}}_{\text{in}}(kh)$ and $\bar{P}_{\text{in}}(kh)$ obtained from all three greyhound experiments ($N = 3$) during healthy conditions (C1), and reduced heart contractility, with low afterload (C2) are illustrated in figures 6(A) and (B), respectively.

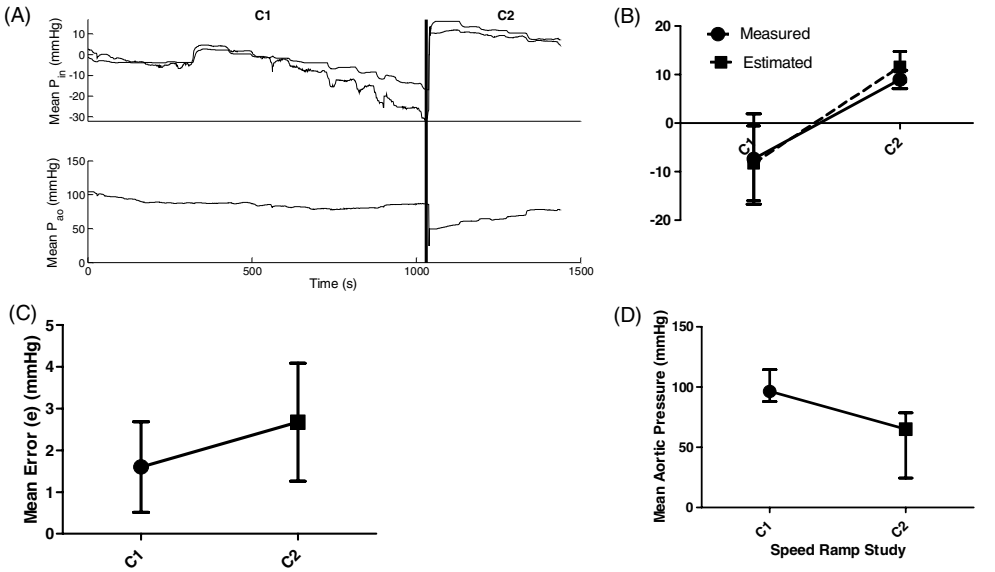

Figure 4. (A) $\hat{\bar{P}}_{\text{in}}(kh)$ compared with $\bar{P}_{\text{in}}(kh)$ obtained from the second greyhound experiment during healthy (C1) and from after heart contractility was reduced by metoprolol infusion (C2) together with (B) comparison between mean estimated versus measured P_{in} during C1 and C2, and (C) comparison between estimation errors obtained during speed ramp tests C1 and C2 in the second greyhound. (D) Mean aortic pressure/afterload variations during speed ramp experiments C1 and C2. Target rotational speed was varied from $\omega = 1250$ to 2950 rpm in both speed ramp tests C1 and C2. The solid line shows the measured $\bar{P}_{\text{in}}(kh)$, while the dashed line shows $\hat{\bar{P}}_{\text{in}}(kh)$.

Table 1. Linear regression analysis results between estimated and measured mean P_{in} from three *in vivo* greyhound experiments during healthy speed ramp test (C1). Results for all animals show mean ± SD where appropriate.

		Parameter			
Experiment	$\bar{P}_{\text{in}}$ (mmHg)	$\hat{\bar{P}}_{\text{in}}$(mmHg)	$\bar{P}_{ao}$(mmHg)	e (mmHg)	R^2
Greyhound 1	5.69	4.65	106.55	1.469	0.973
Greyhound 2	−7.39	−8.25	96.34	1.600	0.958
Greyhound 3	5.62	4.28	129.49	1.743	0.941
All animals	1.308 ± 5.53	0.226 ± 5.35	110.79 ± 16.977	1.604 ± 0.1373	0.957 ± 0.0160

Table 2. Linear regression analysis results between estimated and measured mean P_{in} from three *in vivo* greyhound experiments during reduced heart contractility (C2) in which metoprolol was infused to the animals. Results for all animals show mean ± SD where appropriate.

		Parameter			
Experiment	$\bar{P}_{\text{in}}$ (mmHg)	$\hat{\bar{P}}_{\text{in}}$ (mmHg)	$\bar{P}_{ao}$ (mmHg)	e (mmHg)	R^2
Greyhound 1	11.36	8.66	58.85	2.701	0.977
Greyhound 2	8.98	11.57	65.03	2.676	0.928
Greyhound 3	3.84	6.47	46.63	2.687	0.975
All animals	8.056 ± 3.84	8.90 ± 2.56	56.83 ± 9.364	2.688 ± 0.0124	0.961 ± 0.0277

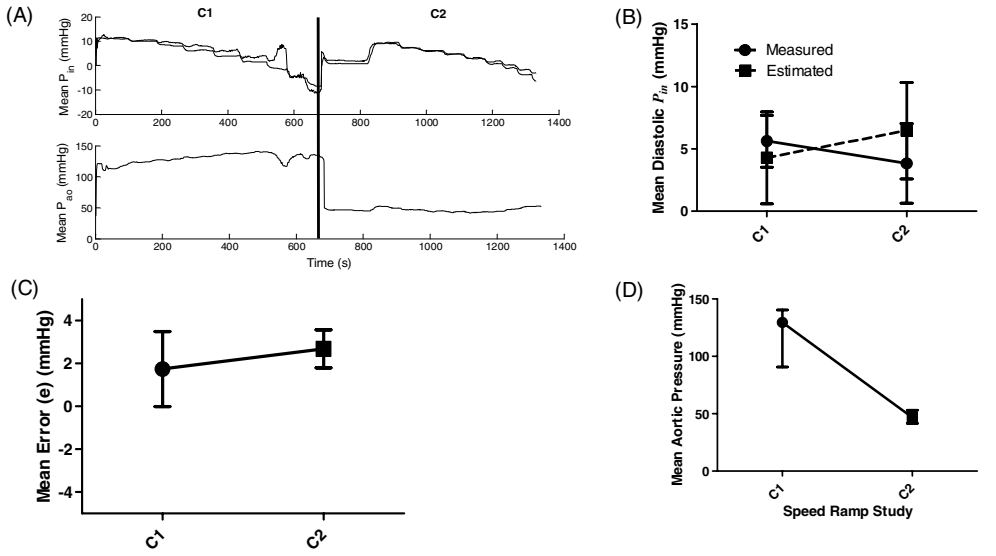

Figure 5. (A) $\hat{\bar{P}}_{\rm in}(kh)$ compared with $\bar{P}_{\rm in}(kh)$ obtained from the third greyhound experiments (C1 and C2) together with (B) comparison between mean measured and estimated $P_{\rm in}$ during C1 and C2, and (C) comparison between estimation errors obtained during speed ramp tests C1 and C2 in the third greyhound experiments. (D) Mean P_{ao} during speed ramp tests C1 and C2, respectively. Also, in this greyhound and during C1 and C2, target rotational speed was varied from $\omega = 1250$ to 2950 rpm during healthy conditions and from after reduced heart contractility was achieved by metoprolol infusion. The solid line shows the measured extracted $\bar{P}_{\rm in}(kh)$, while the dashed line shows $\hat{\bar{P}}_{\rm in}(kh)$.

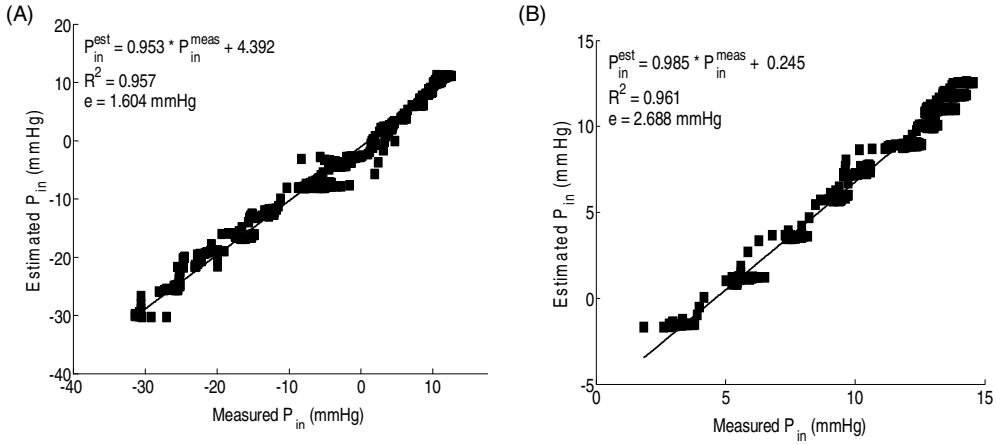

Figure 6. Linear regression plot between $\hat{\bar{P}}_{\rm in}(kh)$ versus $\bar{P}_{\rm in}(kh)$ from all animal data during (A) healthy conditions (C1), and (B) reduced heart contractility-afterload low (C2) where metoprolol was infused. All sets of data ($N = 3$) obtained from each greyhound experiment during speed ramp tests C1 and C2 were concatenated.

During speed ramp test C1, analyzing all greyhound data in the validation set resulted in a highly significant correlation ($R^2 = 0.957$) between estimated and measured $P_{\rm in}$ with a small mean absolute error value ($e = 1.604$ mmHg). The mean slope of the linear regression

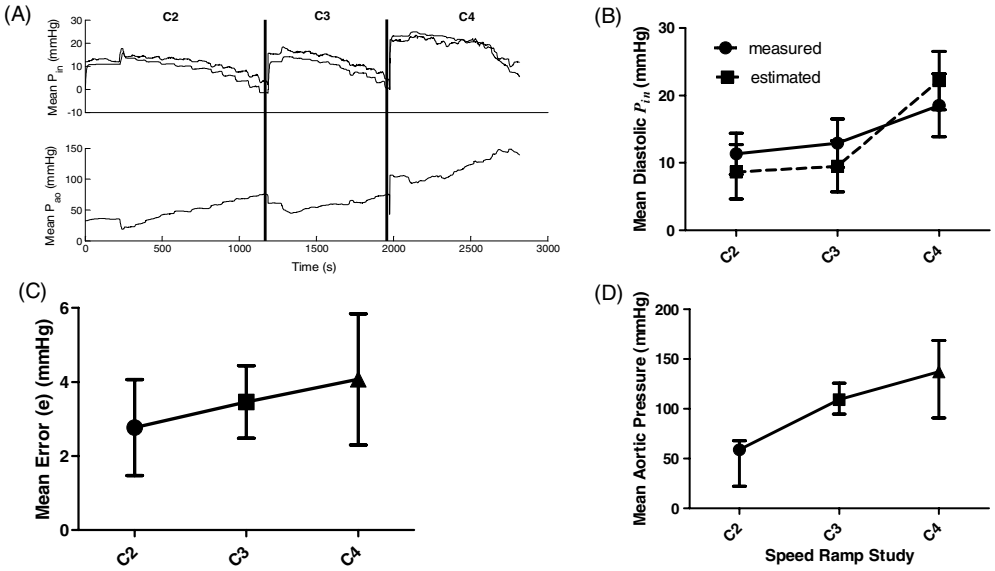

Figure 7. (A) $\hat{\bar{P}}_{\text{in}}(kh)$ compared with $\bar{P}_{\text{in}}(kh)$ obtained from the first greyhound experiments during reduced heart contractility-afterload low (C2), from after metaraminol was infused, with P_{ao} was increased by 20 mmHg, afterload medium (C3), and from after reduced heart contractility-afterload high (C4), together with (B) comparison between estimated versus measured mean P_{in} obtained during C2, C3 and C4, and (C) comparison between estimation errors obtained during speed ramp tests C2, C3, and C4 in the first greyhound. (D) Mean aortic pressure/afterload variations. In speed ramp studies C2, C3 and C4, target rotational speed was varied from $\omega =$ 1250 to 2950 rpm. The solid line shows $\bar{P}_{\text{in}}(kh)$, while the dashed line shows $\hat{\bar{P}}_{\text{in}}(kh)$.

line was close to unity (0.953) with mean offset value of 4.392. Similarly, during speed ramp test C2, analyzing of all greyhound data set resulted in a highly significant correlation ($R^2 =$ 0.961) between $\hat{\bar{P}}_{\text{in}}(kh)$ and $\bar{P}_{\text{in}}(kh)$ with mean absolute error value ($e = 2.688$ mmHg). The mean slope of the linear regression line was close to unity (0.985) with mean offset value of 0.245. Note the increase in e resulted from the variation of afterload during C2.

Similarly, upper panels of figures 7(A), 8(A), and 9(A) show $\hat{\bar{P}}_{\text{in}}(kh)$ versus $\bar{P}_{\text{in}}(kh)$ during speed ramp tests afterload-low (C2), from after metaraminol-afterload medium (C3), and afterload high (C4) in each greyhound experiment, respectively. The variations in the mean aortic pressure ($\overline{P_{ao}}$) for each dog during speed ramp tests C2, C3 and C4 are also shown in the lower panels of figures 7(A), 8(A), and 9(A), respectively. The comparison between $\hat{\bar{P}}_{\text{in}}(kh)$ together with $\bar{P}_{\text{in}}(kh)$ obtained from each greyhound experiment during C2, C3 and C4 is also shown in figures 7(B), 8(B), and 9(B). Mean absolute error (e) during each speed ramp experiment for each greyhound were also compared in figures 7(C), 8(C), and 9(C). In all greyhounds, metaraminol was infused till $\overline{P_{ao}}$ increased by 20 mmHg compared with C2; this increased the left ventricular contractility which caused a significant variation in mean aortic pressure during speed ramp tests C3, and C4 compared with C1 and C2 (figures 7(D), 8(D), and 9(D)). Compared with C2, the high variation in $\overline{P_{ao}}$ was linearly increased in the model estimation error (e) during C3 and C4.

Tables 3 and 4 summarize the values of $\hat{\bar{P}}_{\text{in}}(kh)$ and $\bar{P}_{\text{in}}(kh)$, $\overline{P_{ao}}$, e, together with values of R^2 obtained from each animal experiment during metaraminol infusion-afterload medium (C3) and afterload high (C4) speed ramp studies. Linear regression analysis between measured

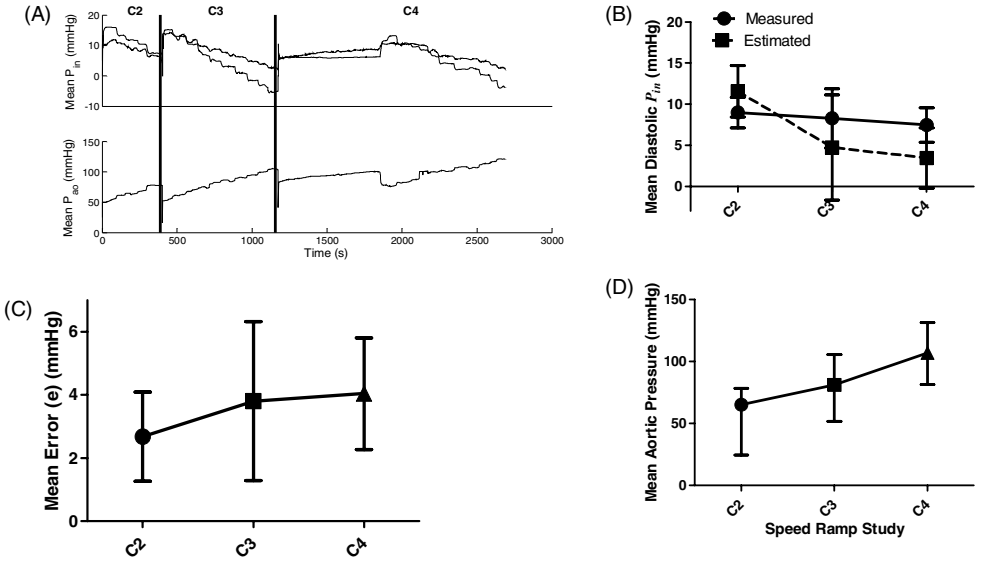

Figure 8. (A) $\hat{\bar{P}}_{\text{in}}(kh)$ compared with $\bar{P}_{\text{in}}(kh)$ obtained from the second greyhound experiments C2, C3, and C4 together with (B) comparison between mean measured and estimated P_{in} during C2, C3, and C4, and (C) comparison between estimation errors obtained during speed ramp tests C2, C3, and C4 in the second greyhound experiments. (D)Variation in mean P_{ao} during speed ramp tests C2, C3 and C4, respectively. Target rotational speed was varied from $\omega = 1250$ to 2950 rpm during C2, C3, and C4. The solid line shows $\bar{P}_{\text{in}}(kh)$, while the dashed line shows $\hat{\bar{P}}_{\text{in}}(kh)$.

Table 3. Linear regression analysis results between estimated and measured mean P_{in} from three *in vivo* greyhound experiments during metaraminol infusion-afterload medium (C3). Results for all animals show mean ± SD where appropriate.

		Parameter			
Experiment	$\bar{P}_{\text{in}}$ (mmHg)	$\hat{\bar{P}}_{\text{in}}$ (mmHg)	$\bar{P}_{ao}$ (mmHg)	e (mmHg)	R^2
Greyhound 1	12.95	9.48	109.17	3.460	0.943
Greyhound 2	8.28	4.73	81.09	3.800	0.985
Greyhound 3	7.10	9.77	87.98	3.741	0.946
All animals	9.443 ± 3.09	7.993 ± 2.83	92.74 ± 14.634	3.667 ± 0.1821	0.958 ± 0.0234

Table 4. Linear regression analysis results between estimated and measured mean P_{in} from three *in vivo* greyhound experiments during C4 in which metaraminol was infused to increase mean P_{ao} by 20 mmHg compared with C3 and caused a high variation in afterload in all animals. Results for all animals show mean ± SD where appropriate.

		Parameter			
Experiment	$\bar{P}_{\text{in}}$ (mmHg)	$\hat{\bar{P}}_{\text{in}}$ (mmHg)	$\bar{P}_{ao}$ (mmHg)	e (mmHg)	R^2
Greyhound 1	18.54	22.22	137.18	4.072	0.947
Greyhound 2	7.46	3.46	106.80	4.037	0.966
Greyhound 3	5.59	9.38	109.81	3.863	0.972
All animals	10.53 ± 6.997	11.68 ± 9.59	117.93 ± 16.741	3.991 ± 0.1120	0.963 ± 0.0130

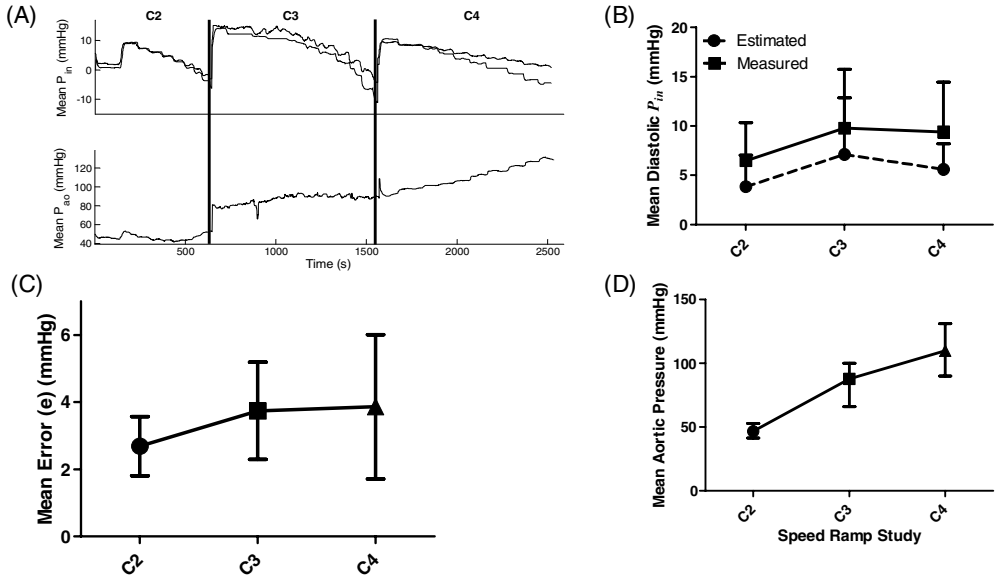

Figure 9. (A) $\hat{\bar{P}}_{\rm in}(kh)$ compared with $\bar{P}_{\rm in}(kh)$ obtained from the third greyhound experiments during C2, C3, and C4 together with (B) comparison between mean measured and estimated $P_{\rm in}$ during C2, C3, and C4, and (C) comparison between estimation errors obtained during speed ramp tests C2, C3, and C4 in the third greyhound experiments. (D) Variations in afterload ($\overline{P_{ao}}$) during speed ramp tests C2, C3, and C4, respectively. Also, during C2, C3, and C4, target rotational speed was varied from $\omega = 1250$ to 2950 rpm. The solid line shows $\bar{P}_{\rm in}(kh)$, while the dashed line shows $\hat{\bar{P}}_{\rm in}(kh)$.

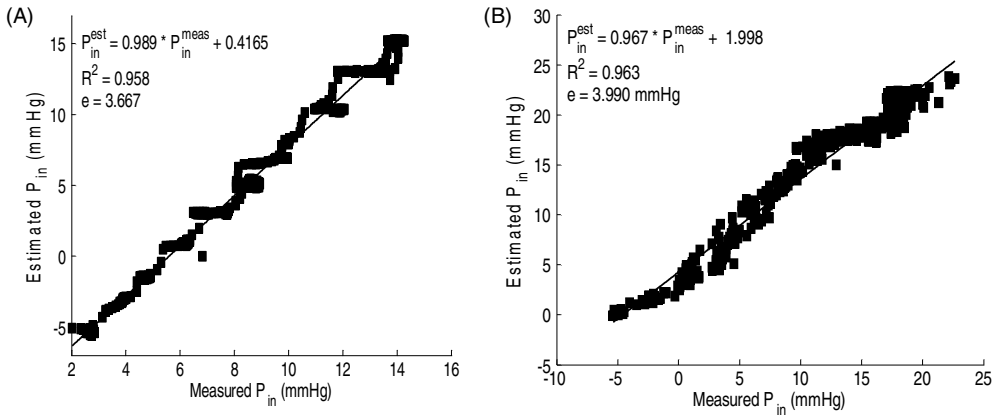

Figure 10. Linear regression plot between $\hat{\bar{P}}_{\rm in}(kh)$ versus $\bar{P}_{\rm in}(kh)$ obtained from all animal data during (A) afterload-medium (C3), and (B) afterload-high (C4). All sets of data ($N = 3$) obtained from each greyhound experiment during speed ramp tests C3 and C4 were concatenated.

and estimated $P_{\rm in}$ obtained from all three greyhound experiments ($N = 3$) during C3, and C4 are also illustrated in figures 10(A) and (B), respectively. During speed ramp test C3, analyzing all greyhound data in the validation set resulted in a highly significant correlation ($R^2 = 0.958$)

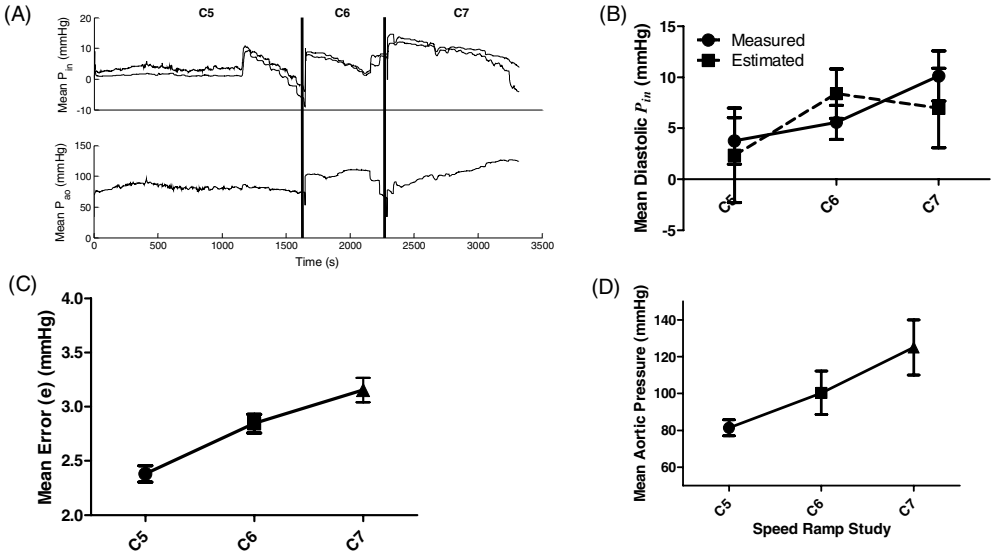

Figure 11. (A) $\hat{\bar{P}}_{\text{in}}(kh)$ compared with $\bar{P}_{\text{in}}(kh)$ obtained from the first greyhound experiments during speed ramp tests preload-low (C5), preload-medium (C6), and preload-high (C7), together with (B) comparison between mean estimated versus mean measured P_{in} obtained during C5, C6 and C7, and (C) comparison between estimation errors obtained during C5, C6, and C7. (D) Mean aortic pressure/afterload ($\overline{P_{ao}}$) variations. In speed ramp studies C5, C6 and C7, target rotational speed was varied from $\omega = 1250$ to 2950 rpm. The solid line shows $\bar{P}_{\text{in}}(kh)$, while the dashed line shows $\hat{\bar{P}}_{\text{in}}(kh)$.

between $\hat{\bar{P}}_{\text{in}}(kh)$ and $\bar{P}_{\text{in}}(kh)$ with mean absolute error value ($e = 3.667$ mmHg). The mean slope of the linear regression line was close to unity (0.989) with mean offset value of 0.4165. Similarly, during speed ramp test C4, analyzing of all greyhound data ($N = 3$) in the validation set resulted in a highly significant correlation ($R^2 = 0.963$) between $\hat{\bar{P}}_{\text{in}}(kh)$ and $\bar{P}_{\text{in}}(kh)$ with mean absolute error value ($e = 3.990$ mmHg). The mean slope of the linear regression line was close to unity (0.967) with mean offset value of 1.998.

The estimated and measured mean diastolic P_{in} during the preload dependence ramp speed studies, where the metaraminol infusion was stopped and from after the rate of the cardiotomy suction system was varied in order to change the total blood volume from low (C5), medium (C6), and high (C7), are shown in the upper panels of figures 11(A), 12(A), and 13(A). The variations in $\overline{P_{ao}}$ for each dog experiment during speed ramp tests C5, C6, and C7 are also shown in the lower panels of figures 11(A), 12(A), and 13(A), respectively. Note that the model was able to accurately track the changes in $\bar{P}_{\text{in}}(kh)$ with stable transient response when preload was varied from low to medium and high. The comparison between $\hat{\bar{P}}_{\text{in}}(kh)$ together with $\bar{P}_{\text{in}}(kh)$ obtained from each greyhound experiment during C5 and C6, and C7 is also shown in figures 11(B), 12(B), and 13(B). The corresponding mean absolute error (e) during each speed ramp test is shown in figures 11(C), 12(C), and 13(C). Moreover, the variations in $\overline{P_{ao}}$ during C5, C6, and C7 are also shown in figures 11(D), 12(D), and 13(D), respectively.

Linear regression analysis between $\hat{\bar{P}}_{\text{in}}(kh)$ and $\bar{P}_{\text{in}}(kh)$ obtained from all three greyhound experiments ($N = 3$) during preload dependence speed ramp studies C5, C6, and C4 are also illustrated in figures 14(A)–(C), respectively. During speed ramp test C5, analyzing all

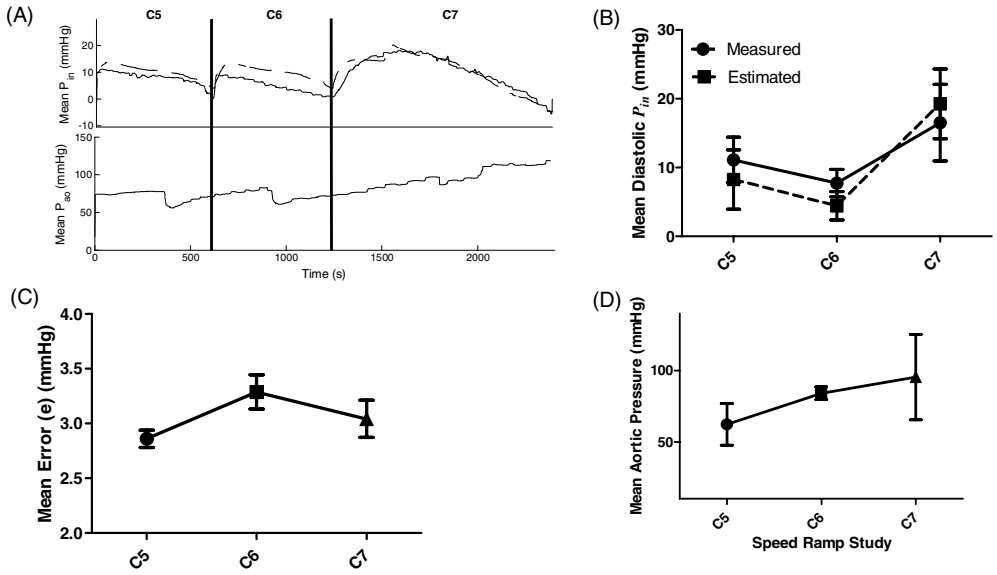

Figure 12. (A) $\hat{\bar{P}}_{\text{in}}(kh)$ compared with $\bar{P}_{\text{in}}(kh)$ obtained from the second greyhound experiments during C5, C6, and C7 together with (B) comparison between mean measured and estimated P_{in} during C5, C6, and C7, and (C) comparison between estimation errors obtained during speed ramp tests C5, C6, and C7 in the second greyhound experiment. (D) Variations in $\overline{P_{ao}}$ during speed ramp tests. Target rotational speed was varied from $\omega = 1250$ to 2950 rpm. The solid line shows $\bar{P}_{\text{in}}(kh)$, while the dashed line shows $\hat{\bar{P}}_{\text{in}}(kh)$.

greyhound data ($N = 3$) in the validation set resulted in a highly significant correlation ($R^2 = 0.940$) between $\hat{\bar{P}}_{\text{in}}(kh)$and $\bar{P}_{\text{in}}(kh)$ with mean absolute error value ($e = 2.791$ mmHg). The mean slope of the linear regression line was close to unity (1.146) with mean offset value of -0.892. Similarly, during speed ramp test C6, analyzing of all greyhound data ($N = 3$) in the validation set resulted in a highly significant correlation ($R^2 = 0.946$) between $\hat{\bar{P}}_{\text{in}}(kh)$ and $\bar{P}_{\text{in}}(kh)$ with mean absolute error value ($e = 3.215$ mmHg). The mean slope of the linear regression line was close to unity (1.077) with mean offset value of 2.38. Also, $R^2 = 0.959$, $e = 3.225$ mmHg, mean slope of the linear regression line equals 1.042, and mean offset values of 2.652 were obtained from analyzing all data sets in the validation set ($N = 3$) during speed ramp study C7. Tables 5–7 summarize the values of mean estimated and measured P_{in}, $\overline{P_{ao}}$, e, together with values of correlation coefficient (R^2) obtained from each animal experiment during blood volume changes, preload dependence studies, C5, C6, and C7, respectively.

Parameter coefficients of the system models described in equations (14) and (15) which were used for two-step ahead prediction and to simulate values of mean pump power and rotational speed are listed in tables 8 and 9, respectively. Values of these coefficients were identified using the system identification algorithm previously described in subsection 2.3. Figure 15(A) shows $\hat{\bar{P}}(kh)$ together with $\bar{P}(kh)$. Linear regression analysis between $\hat{\bar{P}}(kh)$ and $\bar{P}(kh)$ resulted in a high correlation coefficient ($R^2 = 0.969$) with small mean absolute error ($e = 0.451$ W). The mean slope of the linear regression line is also close to unity (0.9439). A linear regression plot between $\hat{\bar{P}}(kh)$ and actual $\bar{P}(kh)$ is shown in figure 15(B).

Similarly, $\hat{\bar{\omega}}(kh)$ represented by equation (15), versus the actual one $\bar{\omega}(kh)$ is shown in figure 16(A). Furthermore, linear regression analysis between $\hat{\bar{\omega}}(kh)$ and $\bar{\omega}(kh)$ resulted in

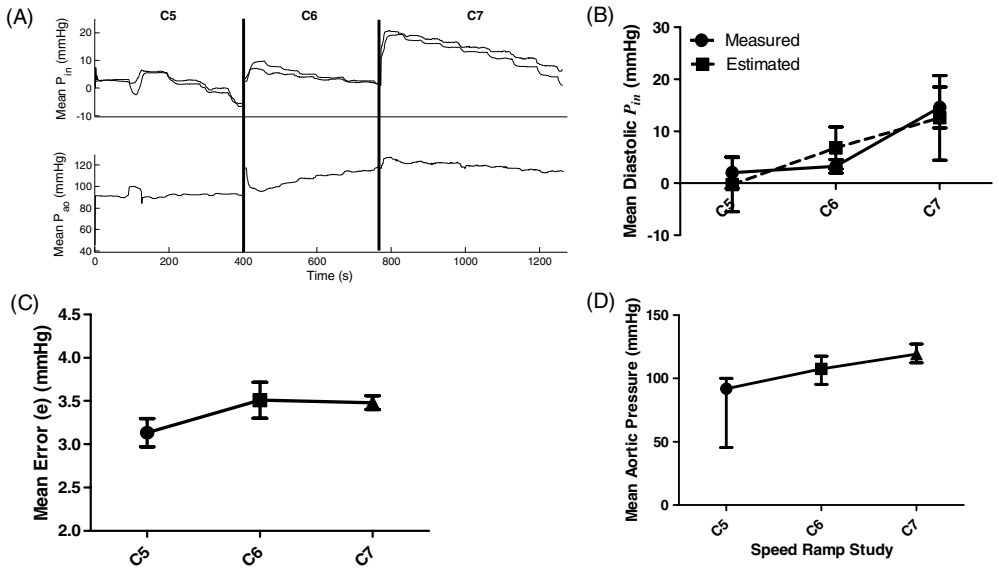

Figure 13. (A) $\hat{\bar{P}}_{\text{in}}(kh)$ compared with $\bar{P}_{\text{in}}(kh)$ obtained from the third greyhound experiments during C5, C6, and C7 together with (B) comparison between mean measured and estimated P_{in} during C5, C6, and C7, and (C) the estimation errors obtained during speed ramp tests C5, C6, and C7. (D) Variations in $\overline{P_{ao}}$. Here, target rotational speed was also varied from $\omega = 1250$ to 2950 rpm. The solid line shows $\bar{P}_{\text{in}}(kh)$, while the dashed line shows $\hat{\bar{P}}_{\text{in}}(kh)$.

Table 5. Linear regression analysis results between estimated and measured mean diastolic P_{in} from three *in vivo* greyhound experiments during preload low ramp study (C5). Results for all animals show mean ± SD where appropriate.

		Parameter			
Experiment	$\bar{P}_{\text{in}}$ (mmHg)	$\hat{\bar{P}}_{\text{in}}$ (mmHg)	$\bar{P}_{ao}$ (mmHg)	e (mmHg)	R^2
Greyhound 1	3.76	2.35	81.47	2.381	0.966
Greyhound 2	11.11	8.26	62.35	2.860	0.946
Greyhound 3	2.06	−0.26	91.97	3.133	0.910
All animals	5.643 ± 8.135	3.45 ± 4.364	78.59 ± 15.012	2.791 ± 0.3809	0.940 ± 0.0283

Table 6. Linear regression analysis results between estimated and measured mean diastolic P_{in} from three *in vivo* greyhound experiments during preload medium ramp study (C6). Results for all animals show mean ± SD where appropriate.

		Parameter			
Experiment	$\bar{P}_{\text{in}}$ (mmHg)	$\hat{\bar{P}}_{\text{in}}$ (mmHg)	$\bar{P}_{ao}$ (mmHg)	e (mmHg)	R^2
Greyhound 1	5.57	8.38	100.39	2.85	0.947
Greyhound 2	7.70	4.41	84.18	3.29	0.948
Greyhound 3	3.28	6.78	107.51	3.51	0.943
All animals	5.52 ± 2.210	6.523 ± 1.997	97.36 ± 11.954	3.217 ± 0.3376	0.946 ± 0.0026

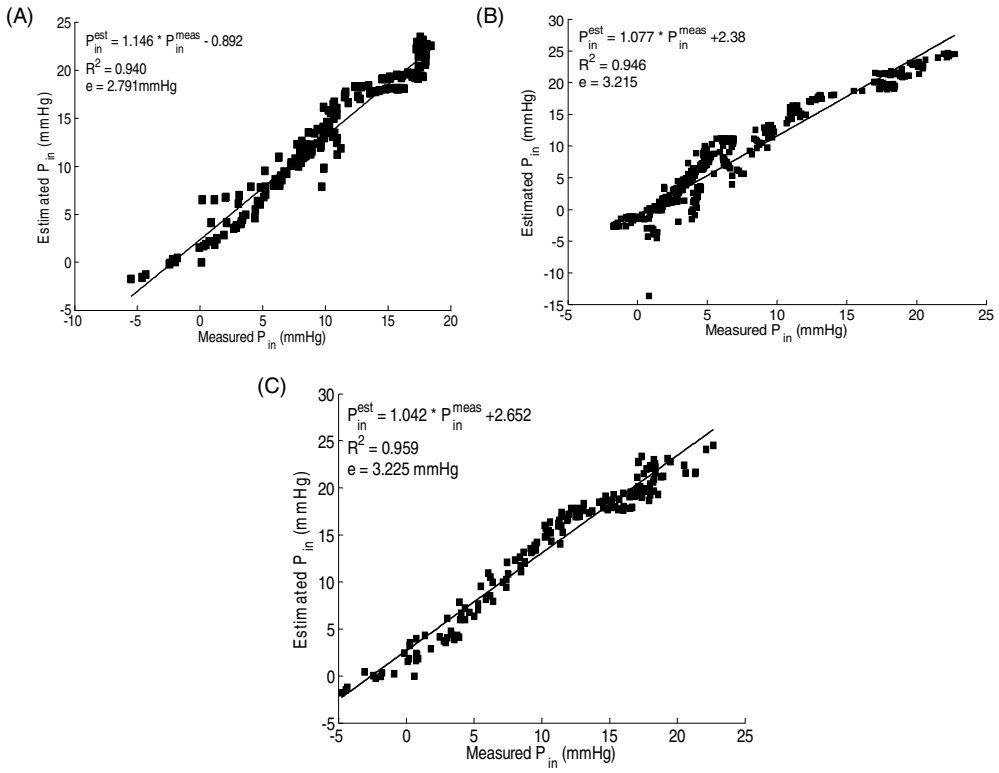

Figure 14. Linear regression plot between $\hat{\bar{P}}_{\text{in}}(kh)$versus $\bar{P}_{\text{in}}(kh)$ obtained from all animal data ($(N = 3)$) during three distinct blood volume changes (A) preload-low (C5), and (B) preload-medium (C6), and (C) preload-high (C7). All sets of data obtained from each greyhound experiment during speed ramp test C5, C6, and C7 were concatenated.

Table 7. Linear regression analysis results between estimated and measured mean P_{in} from three *in vivo* greyhound experiments during preload high ramp study (C7). Results for all animals show mean ± SD where appropriate.

		Parameter			
Experiment	$\bar{P}_{\text{in}}$ (mmHg)	$\hat{\bar{P}}_{\text{in}}$ (mmHg)	$\bar{P}_{ao}$ (mmHg)	e (mmHg)	R^2
Greyhound 1	10.13	6.97	125.05	3.15	0.955
Greyhound 2	16.51	19.26	95.54	3.04	0.956
Greyhound 3	14.58	12.59	119.19	3.48	0.966
All animals	13.74 ± 3.275	12.94 ± 6.14	113.26 ± 15.623	3.225 ± 0.2281	0.959 ± 0.0060

a high correlation coefficient ($R^2 = 0.975$) and small mean absolute error ($e = 14.79$ rpm). The slope of the regression line was very close to unity (0.9914) with an offset value of 26.39 rpm. A graph of linear regression between simulated and actual pump rotational speeds is illustrated in figure 16(B).

In this study, the models developed for estimation of mean diastolic inlet pressure ($\hat{\bar{P}}_{\text{in}}(kh)$) described in equation (16), extracted $\bar{P}(kh)$, $\bar{\omega}(kh)$, $\bar{f}(kh)$ during T_d, together with the control signal described in equation (17) were used to design a control algorithm

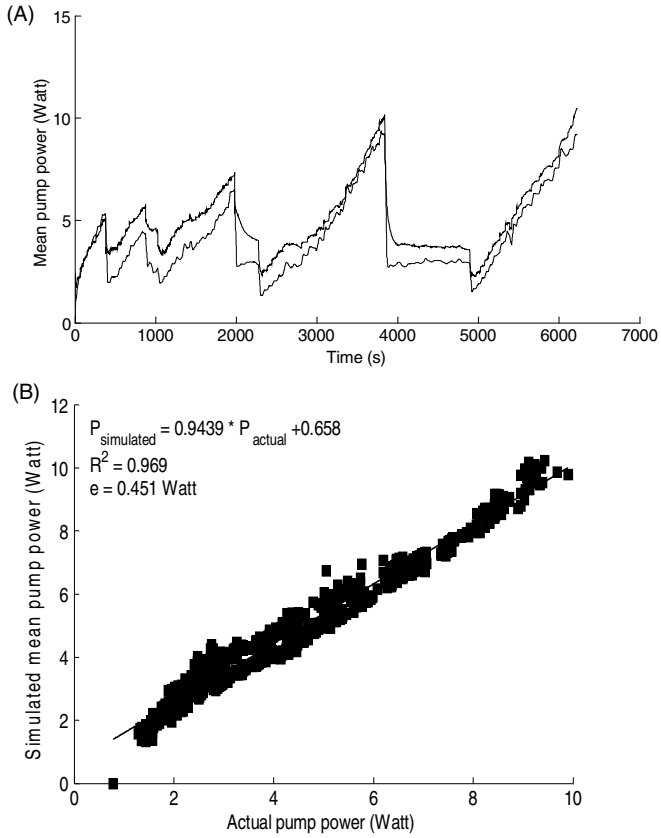

Figure 15. (A) Simulated mean motor power compared with actual. Data were concatenated to facilitate the study of the transient response of the model. The simulated mean pump power as per equation (14) was able to track the changes in motor power. The solid line shows the actual pump power, while the dashed line shows the simulated motor power during the diastolic period (T_d). (B) Linear regression plot between simulated versus actual pump power obtained from dog data ($N = 3$).

to control $\hat{\bar{P}}_{\text{in}}(kh)$ during T_d. The simulation was first carried out using varying levels of constant reference mean diastolic inlet pressure of the pump. Next, square wave signals of varying mean, amplitude and duty cycles were applied to the reference input, $r(kh)$, of the controller shown in figure 2 to mimic the variable nature of inlet pressure. Figure 17 shows the resulting output against the desired reference input where the amplitude of the simulated mean diastolic inlet pressure of the pump was assumed to change between ± 10 mmHg for each heart period. It was shown that the simulated mean inlet pressure accurately tracked the reference input signal within an error of ± 0.92 mmHg.

4. Discussion

The issues of non-invasive estimation and control of inlet pressure in IRBPs have not been frequently studied. This may be due to the highly variable nature of pump parameters including pump flow, speed, current and the inlet pressure, especially during abnormal pumping states of the pump such as ventricular suction.

Table 8. Values of the parameter coefficients for the system model, used to simulate mean pump power during the diastolic period (T_d) of the cardiac cycle, as shown in equation (14).

Coefficient	Value
d_1	0.107
d_2	0.0925
d_3	0.000 62
d_4	0.000 44
d_5	0.0365
d_6	0.021 83
d_7	0.003 06
d_8	0.002 02
d_9	1.369 00
d_{10}	0.675 10
d_{11}	0.283 00

Table 9. Values of the parameter coefficients for the system model, used to simulate mean rotational pump speed during the diastolic period (T_d) of the cardiac cycle, as shown in equation (15).

Coefficient	Value
g_1	2.865
g_2	3.026
g_3	20.740
g_4	26.660
g_5	12.890
g_6	8.616
g_7	1.182
g_8	1.210
g_9	1.593
g_{10}	0.7055

In this study, a dynamical model for mean inlet pressure estimation during the diastolic period was successfully designed and verified against experimental data. The model was then used by way of computer simulations to test the response of a deadbeat controller for control and regulation of the mean inlet pressure during the diastolic period. The preliminary results presented in the current study have explored the interaction and relationship between non-invasive measurements of the IRBP such as pump rotational speed, motor power, together with PWM signal and the pump inlet pressure during diastole, thus providing a measure of left ventricular preload.

Monitoring of the pump inlet pressure plays a vital role in controlling the operation of the IRBPs. Firstly, it makes ventricular suction detection easier. When suction occurs, the inlet pressure decreases to less than zero mmHg (as low as −160 mmHg). This is caused by the adjacent ventricular wall transiently obstructing the pump inlet. When this occurs, pump flow decreases eventually to zero in cases of severe suction. This causes a large negative pressure spike significantly below the normal fall in diastole. It has been proposed that the width of the negative spike during diastole is equal to the suction duration (Saito *et al* 2010).

The second major advantage of inlet pressure monitoring is its great value in the regulation of pump flow. During normal diastole, the inlet pressure and left ventricular end diastolic

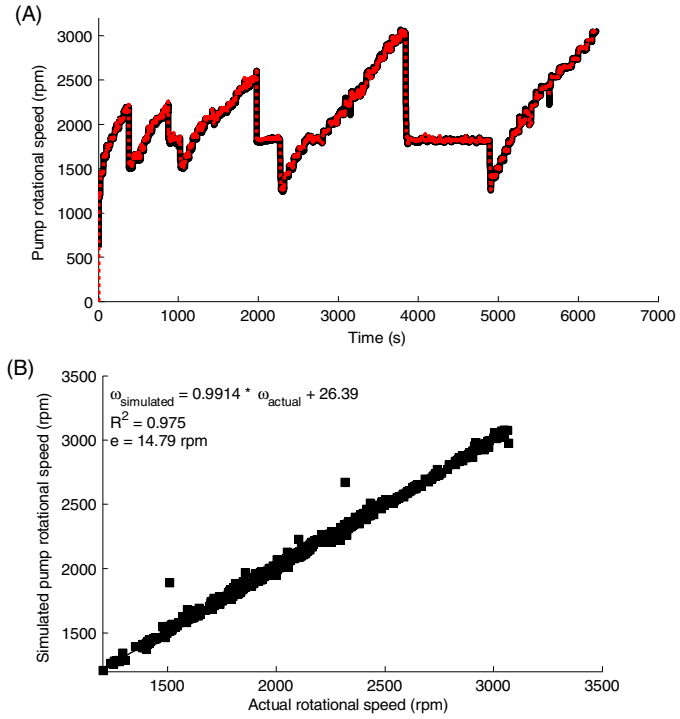

Figure 16. (A) Simulated pump rotational speed compared with the actual one during the diastolic period (T_d). The target rotational speed was varied from $\omega = 1250$ to 2950 rpm during each blood volume change. Data were concatenated so that it was easy to study the transient response of the model. The solid line shows the actual rotational pump speed, while the dashed red line shows the simulated mean rotational speed during the diastolic period. (B) Linear regression plot between simulated versus actual pump power obtained from dog data ($N = 3$).

(This figure is in colour only in the electronic version)

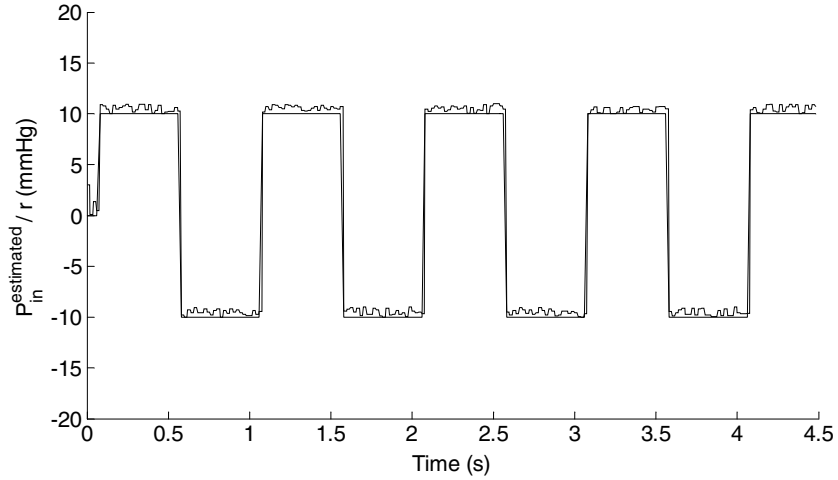

Figure 17. Desired reference input r, shown as solid line, versus the response of mean diastolic inlet pressure controller shown as dashed line.

pressure are closely related. At the end of diastole, this pressure equates to left ventricular preload. For a fixed inotropic heart state, this pressure and the associated ventricular volume are the most important factors regulating the force of ventricular contraction and the consequent stroke volume. The precise relationship between ventricular preload and stroke work is defined as the Frank–Starling law (Guyton and Hall 1996). This is the major mechanism underlying the synchronization of left and right heart outputs which in steady state is mandatory (Mohrman and Heller 2006). Lack of this synchronization as in IRBPs, which do not have an inherent Starling characteristic, can give rise to a number of consequences, the most serious being ventricular suction.

Non-invasive estimation and control of inlet pressure during diastole is thus of considerable benefit. It facilitates the design of preload controllers of varying sophistication, the simplest being the maintenance of a set end-diastolic pressure. A more sophisticated alternative is to control the pump flow so that its output relates to the end-diastolic pressure as defined by the Frank–Starling mechanism. This would allow the pump to achieve a range of flows and left ventricular preloads in dynamic equilibrium with other changes in the patient's hemodynamic state. Suction would be avoided with both these strategies.

The methods presented in this study are sufficiently accurate and stable to operate effectively in the clinical environment thus enabling non-invasive monitoring and control of left ventricular preload. It consequently avoids the use of one implantable pressure transducer (Bullister *et al* (2002)) or perhaps two (Giridharan *et al* (2002)). At the moment, commercially available pressure transducers are unsuitable for the task because of excessive drift, and mechanical unreliability. Although more stable transducers are in prototype form, they are not yet ready for commercial development (Najafi and Ludomirsky 2004, Chow *et al* 2010).

5. Study limitations

One limitation of the current study is that in a VentrAssist^{TM} LVAD, the power coefficient values used in the static flow estimator equation (5) as well as our estimation models were affected by the HCT values. This required routine measurement of the HCT during the experiment and adjustment of the model as described in Malagutti *et al* (2007). Further research of online estimation of HCT is being conducted in our laboratory.

The P_{in} estimation model showed a stable response during speed ramp studies C1–C7 in the presence of highly significant variations in mean aortic pressure/afterload and was able to track the measured extracted signal with minimum mean absolute error during healthy conditions (C1). With the other conditions C2–C7, the mean absolute error (e) between the estimated and measured mean inlet pressure increased likely influenced by a significantly more variable mean aortic pressure. Further investigations are needed into the response of the proposed model and the controller under a highly variable aortic pressure/afterload.

Moreover, the proposed model only estimates the mean inlet pressure during the diastolic period which is almost a piecewise constant line varies between ± 10 mmHg during healthy conditions and can go up to ± 20 mmHg in greyhound experiment 1 during C4, and in greyhound dog experiment 2 during C7. Other inputs may be needed to estimate the systolic inlet pressure.

6. Conclusion and future research

A novel and stable dynamical model was proposed for mean inlet pressure estimation during the diastolic period in an IRBP. In the proposed model, non-invasive measurements of motor power

and impeller rotational speed were used as inputs. The model was able to track the measured signal with stable transient response during different operating conditions including healthy, reduced heart contractility, variations in aortic pressure/afterload, and preload. Furthermore, in this paper, we developed a non-invasive controller that controls the mean inlet pressure during the diastolic period. The performance of the controller was tested in the presence of model uncertainty. Simulation results showed that the controller was able to track the reference input with minimal error and minimum sampling periods. The controller developed in this paper represents preliminary work on controlling and regulating the diastolic inlet pressure and does not stand alone. Future work will include other more robust control approaches. Also, the proposed controller could play a vital role as a part of the multi-objective physiological controller developed previously in our laboratory (Karantonis *et al* 2010) or as a suction release controller in the pulsatile and continuous flow control algorithm proposed by our research group (Lim *et al* 2010a). On-going work in our laboratory includes testing the model and the controller responses to cardiovascular perturbations and changes in physiological parameters associated with varying forms of simulated heart failure (Lim *et al* 2010b).

Acknowledgment

This work was supported in part by the Australian Research Council.

References

AlOmari A H, Savkin A V, Ayre P J, Lim E and Lovell N H 2010 Sensorless estimation of inlet pressure in implantable rotary blood pump for heart failure patients *Electron. Lett.* **46** 481–3

AlOmari A H, Savkin A V, Karantonis D M, Lim E and Lovell N H 2009 Non-invasive estimation of pulsatile flow and differential pressure in an implantable rotary blood pump for heart failure patients *Physiol. Meas.* **30** 371–86

Arndt A, Nüsser P, Graichen K, Müller J and Lampe B 2008 Physiological control of a rotary blood pump with selectable therapeutic options: control of pulsatility gradient *Artif. Org.* **32** 761–71

Åström K J and Wittenmark B 1997 *Computer-controlled systems: Theory and Design* 3rd edn (Upper Saddle River, NJ: Prentice-Hall)

Ayre P J, Lovell N H and Woodard J C 2003 Non-invasive flow estimation in an implantable rotary blood pump: a study considering non-pulsatile and pulsatile flow *Physiol. Meas.* **24** 179–98

Bullister E, Reich S and Sluetz J 2002 Physiologic control algorithms for rotary blood pumps using pressure sensor input *Artif. Org.* **26** 931–8

Choi S, Antaki J F, Boston J R and Thomas D A 2001 A sensorless approach to control of a turbodynamic left ventricular assist system *IEEE Trans. Control Syst. Technol.* **9** 473–82

Choi S, Boston J R and Antaki J F 2005 An investigation of the pump operating characteristics as a novel control index for LVAD control *Int. J. Control Autom. Syst.* **3** 100–8

Choi S, Boston J R and Antaki J F 2007 Hemodynamic controller for left ventricular assist device based on pulsatility ratio *Artif. Org.* **31** 114–25

Chow E Y, Chlebowski A L, Chakraborty S, Chappell W J and Irazoqui P P 2010 Fully wireless implantable cardiovascular pressure monitor integrated with a medical stent *IEEE Trans. Biomed. Eng.* **57** 1487–96

Endo G, Araki K, Kojima K, Nakamura K, Matsuzaki Y and Onitsuka T 2001 The index of motor current amplitude has feasibility in control for continuous flow pumps and evaluation of left ventricular function *Artif. Org.* **25** 697–702

Fu M and Xu L 2000 Computer simulation of sensorless fuzzy control of a rotary blood pump to assure normal physiology *ASAIO J.* **46** 273–8

Giridharan G and Skliar M 2006 Physiological control of blood pumps using intrinsic pump parameters: a computer simulation study *Artif. Org.* **30** 301–7

Giridharan G A and Skliar M 2002 Nonlinear controller for ventricular assist devices *Artif. Org.* **26** 980–4

Giridharan G A, Skliar M, Olsen D B and Pantalos G M 2002 Modeling and control of a brushless DC axial flow ventricular assist device *ASAIO J.* **48** 272–89

Guyton A C and Hall J E 1996 *Textbook in Medical Physiology* (Philadelphia, PA: Saunders)

Karantonis D M, Lim E, Mason D G, Salamonsen R F, Ayre P J and Lovell N H 2010 Noninvasive activity-based control of an implantable rotary blood pump: comparative software simulation study *Artif. Org.* **34** E34–45

Lim E, AlOmari A H, Savkin A V and Lovell N H 2009 Noninvasive deadbeat control of an implantable rotary blood pump: a simulation study *Proc. 31st Annu. Int. Conf. of the IEEE Eng. Med. Biol. Soc.* pp 2855–8

Lim E, AlOmari A H, Savkin A V, Mason D G, Fraser J F, Gaddum N and Lovell N H 2010a A method for control of an implantable rotary blood pump for heart failure patients using non-invasive measurements *Artif. Org.* at press

Lim E, Dokos S, Cloherty S L, Salamonsen R F, Mason D G, Reizes J A and Lovell N H 2010b Parameter-optimized model of cardiovascular-rotary blood pump interactions *IEEE Trans. Biomed. Eng.* **57** 254–66

Ljung L 1999 *System Identification: Theory for the User* 2nd edn (Englewood Cliffs, NJ: Prentice-Hall)

Malagutti N, Karantonis D M, Cloherty S L, Ayre P J, Mason D G, Salamonsen R F and Lovell N H 2007 Non-invasive average flow estimation for an implantable rotary blood pump: a new algorithm incorporating the role of blood viscosity *Artif. Org.* **31** 45–52

Mohrman D E and Heller L J 2006 *Cardiovascular Physiology* 6th edn (New York: McGraw-Hill)

Najafi N and Ludomirsky A 2004 Initial animal studies of a wireless, batteryless, MEMS implant for cardiovascular applications *Biomed. Microdevices* **6** 61–5

Saito I, Ishii K, Isoyama T, Ono T, Nakagawa H, Shi W, Inoue Y and Abe Y 2010 Preliminary study of physiological control for the undulation pump ventricular assist device *Proc. 32nd Annu. Int. Conf. of the IEEE Eng. Med. Biol. Soc.* pp 5218–21

Slaughter M S *et al* HeartMate II Investigators 2009 Advanced heart failure treated with continuous-flow left ventricular assist device *N. Engl. J. Med.* **23** 2241–51

Vollkron M, Schima H, Huber L, Benkowski R, Morello G and Wieselthaler G 2005 Development of a reliable automatic speed control system for rotary blood pumps *J. Heart Lung Transplant.* **24** 1878–85

Wakisaka Y *et al* 1997 Noninvasive pump flow estimation of a centrifugal blood pump *Artif. Org.* **21** 651–4

Waters T, Allaire P, Tao G, Adams M, Bearnson G, Wei N, Hilton E, Baloh M, Olsen D and Khanwilkar D 1999 Motor feedback physiological control for a continuous flow ventricular assist device *Artif. Org.* **23** 480–6

Wu Y, Allaire P, Tao G, Wood H, Olsen D and Tribble C 2003 An advanced physiological controller design for a left ventricular assist device to prevent left ventricular collapse *Artif. Org.* **27** 926–30

Wu Y, Allaire P E, Tao G, Adams M, Liu Y, Wood H and Olsen D B 2004 A bridge from short-term to long-term left ventricular assist device—experimental verification of a physiological controller *Artif. Org.* **28** 927–32

Wu Y, Allaire P E, Tao G and Olsen D 2007 Modeling, estimation, and control of human circulatory system with a left ventricular assist device *IEEE Trans. Control Syst. Technol.* **15** 754–67

Yoshizawa M, Sato T, Tanaka A, Abe K, Takeda H, Yambe T, Nitta S and Nosé Y 2002 Sensorless estimation of pressure head and flow of a continuous flow artificial heart based on input power and rotational speed *ASAIO J.* **48** 443–8

Zhang X T, AlOmari A H, Savkin A V, Ayre P J, Lim E, Salamonsen R F, Rosenfeldt F L and Lovell N H 2010 *In vivo* validation of pulsatile flow and differential pressure estimation models in a left ventricular assist device *Proc. 32nd Annu. Int. Conf. of the IEEE Eng. Med. Biol. Soc.* pp 2517–20

Zhou J, Armstrong G P, Medvedev A L, Smith W A, Golding L A and Thomas J D 1999 Numeric modeling of the cardiovascular system with a left ventricular assist device *ASAIO J.* **45** 83–9

Zong W, Heldt T, Moody G B and Mark R G 2003 An open-source algorithm to detect onset of arterial blood pressure pulses *Comput. Cardiol.* **30** 259–62